A DIRECT D-BAR METHOD FOR PARTIAL BOUNDARY DATA ELECTRICAL IMPEDANCE TOMOGRAPHY WITH A PRIORI INFORMATION

M. ALSAKER, S. J. HAMILTON, AND A. HAUPTMANN

Abstract. Electrical Impedance Tomography (EIT) is a non-invasive imaging modality that uses surface electrical measurements to determine the internal conductivity of a body. The mathematical formulation of the EIT problem is a nonlinear and severely ill-posed inverse problem for which direct D-bar methods have proved useful in providing noise-robust conductivity reconstructions. Recent advances in D-bar methods allow for conductivity reconstructions using EIT measurement data from only part of the domain (e.g., a patient lying on their back could be imaged using only data gathered on the accessible part of the body). However, D-bar reconstructions suffer from a loss of sharp edges due to a nonlinear low-pass filtering of the measured data, and this problem becomes especially marked in the case of partial boundary data. Including *a priori* data directly into the D-bar solution method greatly enhances the spatial resolution, allowing for detection of underlying pathologies or defects, even with no assumption of their presence in the prior. This work combines partial data D-bar with *a priori* data, allowing for noise-robust conductivity reconstructions with greatly improved spatial resolution. The method is demonstrated to be effective on noisy simulated EIT measurement data simulating both medical and industrial imaging scenarios.

1. Introduction

In Electrical Impedance Tomography (EIT), we measure the surface voltages resulting from the injection of currents on an array of electrodes placed on the surface of a body. These measured boundary currents and voltages are then used to reconstruct the internal electrical conductivity distribution via a mathematical inversion process, thus forming an image of the body's interior structures. Compared with other imaging modalities, EIT has advantages in its low cost, high contrast, portability, and absence of ionizing radiation. There is an ever-growing list of applications of EIT in diverse fields, including medicine and biology, geophysical imaging, process engineering, and nondestructive testing, just to name a few. Of special relevance to the examples studied in this paper are the use of 2-D EIT in human pulmonary imaging, as described for example in [8, 16, 32, 43, 44, 45], along

Date: November 3, 2016.

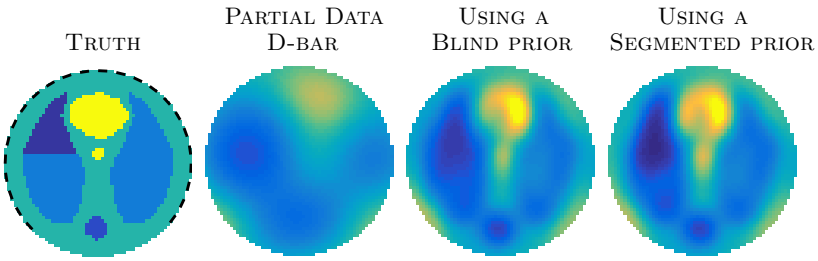

FIGURE 1. Example simulating a patient with a pneumothorax in the left lung. The simulated noisy measurement is collected from 75% ventral data. The first image displays the true conductivity with the position of electrodes indicated. Using a partial data D-bar approach alone results in a reconstruction with low spatial resolution, where the pathology can be hardly seen (second). Incorporating *a priori* data corresponding to a healthy patient directly into the reconstruction method significantly improves the spatial resolution (third). Refining the prior improves the reconstruction further, allowing even sharper visualization of the pathology (fourth).

with the nondestructive testing and evaluation of concrete and other materials in industrial and engineering applications [10, 18, 25, 26, 33, 34, 46]. In these applications, it is of immense interest to detect emerging pathologies when monitoring patients, or defects in industrial components.

In 2-D EIT, electrodes are arranged in a plane around the circumference of the domain, and the reconstruction occurs in the plane of the electrodes. Ideally, electrodes are positioned around the entire boundary, resulting in full boundary data. However, there are many practical applications in which only part of the domain boundary is accessible, and we must rely instead on partial boundary data. This often occurs in medical applications when a critically ill patient is lying on their back and cannot be moved, or in industrial testing applications when, for example, we wish to test a component that is attached to part of a larger structure. Direct D-bar inversion techniques for full boundary data are a well-established category of reconstruction methods based on the results of [41] and [42]. The first practical implementation was described in [47], the method was further developed [38, 30, 11], and a regularization strategy for D-bar methods was introduced and proven in [35]. Furthermore, D-bar reconstruction methods preserve the nonlinearity of the inverse problem, have been proven to exhibit robustness to domain shape errors [40], and are capable of real time imaging [13].

D-bar methods for the partial boundary setting differ from the full boundary case in a few important ways. This study is based on a recently proposed approach in [22], where the authors use a formulation of the conductivity

equation with Neumann boundary conditions corresponding to applied currents. For an open and bounded domain $\Omega \subset \mathbb{R}^2$, with an open (and not necessarily connected) subset $\Gamma \subset \partial\Omega$ on which zero-mean current $\varphi \in L^2(\partial\Omega)$ is injected, the electric potential u supported in Ω is modeled by

$$\begin{aligned} \nabla \cdot \sigma \nabla u &= 0, \quad \text{in } \Omega, \\ \sigma\, \partial_\nu\, u &= \varphi, \quad \text{on } \Gamma \subset \partial\Omega \\ \sigma\, \partial_\nu\, u &= 0, \quad \text{on } \partial\Omega \backslash \Gamma. \end{aligned} \tag{1.1}$$

For uniqueness we require $\int_{\partial\Omega} u \, ds = 0$, and due to conservation of charge $\int_{\partial\Omega} \varphi \, ds = 0$. The resulting voltage distribution on the boundary, $u|_{\partial\Omega}$, is assumed to be known only on Γ. In EIT, we wish to recover the conductivity σ from the boundary measurements $u|_{\partial\Omega}$ and our knowledge of φ.

The boundary data for the EIT problem is given by the Neumann-to-Dirichlet (ND) map, which takes boundary currents to boundary voltages. In the case of full boundary data, where $\Gamma = \partial\Omega$, the computation of the *scattering transform*, which is a nonlinear custom Fourier transform crucial to the method, depends instead on the Dirichlet-to-Neumann (DN) map. In the full boundary setting, the DN map is obtained by simply inverting the ND map. Since the ND data and the DN data are not equivalent for the partial boundary setting, due to the graphs of the operators representing different subsets of the Cauchy data, we cannot use the classical D-bar method that depends on the DN map. For this reason we compute the scattering transform directly from the ND map by an approximation. Details of our setting are discussed in §2. The uniqueness question for the Neumann-to-Dirichlet problem (1.1) has been addressed for coinciding measurement and input domains in $\mathbb{R}^2$ in [29], and in higher dimensions in [21], for bisweep data in [28], and for different input and measurement domains in [7].

Regardless of the reconstruction method used, EIT imaging involves solving a nonlinear and extremely ill-posed inverse problem which requires regularization, so EIT images in general tend to exhibit a loss of sharp edges and finer detail in the presence of noisy measurements. In D-bar methods, this regularization involves low-pass filtering of the nonlinear scattering transform data. Higher scattering frequencies become unstable in the presence of noise and are therefore omitted from the reconstruction process. However, these higher frequencies also encode finer details and sharp edges, and thus the reconstructions suffer from a loss of spatial resolution. These problems are exacerbated in the case of partial boundary data, where, as shown in [22], the introduced error to the reconstruction depends linearly on the missing domain.

One means of improving spatial resolution in EIT reconstructions is the inclusion of prior information in the reconstruction algorithm. This information, in the form of approximate shapes and locations of internal structures and/or regional conductivity estimates, may be obtained in various ways depending on the application. In the case of medical imaging, the approximate shapes, sizes, and locations of organ boundaries may be obtained from

a previous CT or ultrasound scan, or by consulting an anatomical atlas. In particular, in cases where chronically ill patients must receive CT scans as part of a regular course of diagnosis and treatment, these prior scans may be used as a ready source of highly accurate anatomical information for follow-up EIT scans, which do not impart doses of ionizing radiation. For these known structures, conductivity estimates may also be obtained from literature. If instead the application is the nondestructive evaluation of a manufactured structure or machine, the configuration and composition of interior components is likely to be known, and design schematics may be readily available, so that we may obtain spatial information and conductivity estimates for interior structures with great confidence.

In the case of iterative reconstruction algorithms, which typically involve minimizing a cost functional, the use of such *a priori* information—included as a penalty term in the regularization strategy—has been established as a means of enhancing spatial resolution in practical reconstructions, in both medical imaging [2, 3, 6, 12, 14, 15, 31, 48, 49] as well as industrial or engineering applications [23, 24]. In the Bayesian framework the prior distribution is an essential part of the computational inversion. Recent studies employ domain truncation for the partial data problem [4, 5], and region of interest approaches to non-linear difference imaging [36, 37]. A technique for embedding *a priori* information into the D-bar algorithm for full boundary data was introduced in [1], where the method was also proven to be a nonlinear regularization strategy. An analogous method was applied to the D-bar method for full boundary complex admittivity reconstructions in [19]. These methods have been demonstrated to provide noise-robust reconstructions with improved spatial resolution of full boundary simulated human thoracic data, while successfully preserving and enhancing the appearance of introduced pathologies that were not included in the priors.

In this manuscript, the *a priori* D-bar method is extended to the case of conductivity reconstructions from partial boundary data. The purpose of this work is to demonstrate that, even in cases where only partial boundary data is available, *a priori* information can be incorporated into the D-bar method to achieve noise-robust EIT images with enhanced spatial resolution, while preserving data pertaining to previously unknown pathologies or defects, as illustrated in Figure 1. A presentation of the partial boundary problem and D-bar formulation is given in §2, and the new *a priori* method is described in §3. In §4, the effectiveness of the method is demonstrated on noisy data simulating both human thoracic imaging and industrial nondestructive evaluation scenarios. In the case of human thoracic imaging, EIT has been shown to provide information in cases of pneumothorax [9] and pleural effusion [17], and both pathologies are simulated here. For the nondestructive evaluation case, an industrial structural component containing a defect is simulated. In all test cases, only prior information of approximate interior boundaries and conductivity estimates of known structures is included; we do not assume any prior knowledge of pathologies or defects.

This corresponds to a setting in which only prior information pertaining to a healthy or unblemished state is known, but a pathology or defect has developed since the prior information was obtained. The reconstructions demonstrate the effectiveness of the new method to achieve enhanced spatial resolution of not only known internal structures, but also of pathologies and defects not included in the priors. Both full-data and partial-data cases are included for comparison. In §5, final thoughts and conclusions are presented.

2. The partial data problem

The setting of the partial data problem, as we use it, has been introduced in the continuum case in [22]. In the following we will combine this setting with the ideas in [27], such that we model a realistic electrode configuration. The key to the model is a set of well designed projections to the partial boundary, which is represented as a union of electrodes. We consider here a two-dimensional bounded domain $\Omega \subset \mathbb{R}^2$ representing the measured object covered by mutually disjoint electrodes $E_m, m = 1, \ldots, M$. In our computations, we will choose Ω to be the unit disk $\mathbb{D}$. Each electrode is modeled as a connected and open subset of the boundary $\partial\Omega$. The union of all electrodes is denoted as $\Gamma = \cup_m E_m$ and will serve as the domain of current input and voltage measurement. The problem of EIT can then be modeled by the conductivity equation with Neumann boundary conditions as stated in (1.1). The inverse problem is to recover the conductivity $\sigma(x, y)$ for $(x, y) \in \Omega$ from the applied current and resulting voltage measurements on the boundary. The measurement is modeled by the Neumann-to-Dirichlet map (ND map)

$$\mathcal{R}_\sigma : L^2_\diamond(\partial\Omega) \to L^2(\partial\Omega), \quad \mathcal{R}_\sigma\varphi = u|_{\partial\Omega}\,,$$

where $L^2_\diamond(\partial\Omega)$ consists of L^2-functions with zero mean. Thus, the ND map takes every possible current pattern (Neumann data) and maps it to the corresponding voltage distribution on the boundary (Dirichlet data) for a given conductivity distribution σ on Ω. This work focuses on restricted boundary access, only allowing for the measurement of a partial ND map as discussed in [22]. The partial ND map is modeled as the composition of the full-boundary ND map and a bounded linear operator J that maps current patterns $\varphi \in L^2_\diamond(\partial\Omega)$ to a subspace of functions only supported on Γ:

$$L^2_\Gamma(\partial\Omega) := \{\varphi \in L^2_\diamond(\partial\Omega) : \operatorname{supp}(\varphi) = \Gamma \text{ and } \int_\Gamma \varphi = 0\}. \tag{2.1}$$

The partial ND map in this setting is then defined as the composition

$$\mathcal{R}^\Gamma_\sigma := \mathcal{R}_\sigma J,$$

and represents the resulting voltage distribution ideally known on the whole boundary. We will next discuss how to model the input and measurement in the case where the boundary is only partially covered by electrodes.

2.1. **Modeling the measurement process.** Following the construction in [27], we use the concept of extended electrodes $\{\widetilde{E}_m\}_{m=1}^M$ that we define here as open, connected and mutually disjoint subsets of $\partial\Omega$, with the property that

$$E_m \subset \overline{\widetilde{E}}_m \quad \text{and} \quad \bigcup_{m=1}^{M} \overline{\widetilde{E}}_m = \partial\Omega, \quad \text{for } m = 1, \dots, M.$$

Typically, one can only apply discrete current values and, for each applied value, measure one corresponding value for the resulting voltage on each electrode. Thus, we need to produce piecewise constant functions to properly model the input and measurement for an electrode setting. The projections that are presented in the following were introduced in [27] and serve exactly this purpose.

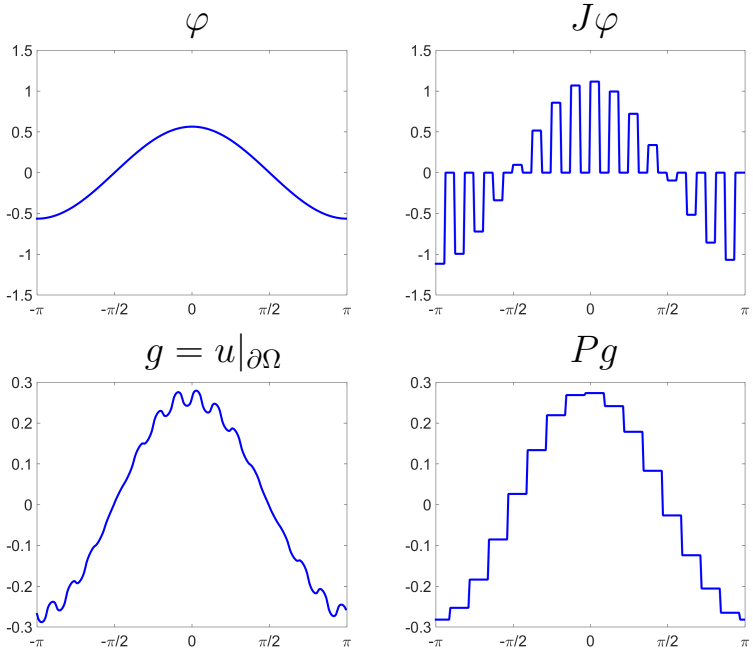

FIGURE 2. Illustration of mappings involved in the measurement modeling. Top row: Neumann data with the basis function $\varphi(\theta) = \cos(\theta)/\sqrt{\pi}$ on the left and the nonorthogonal projection $J\varphi$ on the right. Bottom row: Dirichlet data where $g = u|_{\partial\Omega}$ on the left is the solution of the partial differential equation (1.1) and on the right the orthogonal projection to the extended electrodes.

Let χ_m denote the indicator function for electrode E_m, and analogously $\widetilde{\chi}_m$ for the extended electrodes $\widetilde{E}_m$. Then the partial boundary map that produces the current input is given by a nonorthogonal projection onto the

area of each electrode

$$J : \varphi \mapsto \sum_{m=1}^{M} \frac{\chi_m}{|E_m|} \int_{\widetilde{E}_m} \varphi \, ds, \quad L^2_\diamond(\partial\Omega) \to L^2_\Gamma(\partial\Omega). \tag{2.2}$$

This models the current input on each electrode. To model the voltage measurement process appropriately, we use a projection to extended electrodes with

$$P : g \mapsto \sum_{m=1}^{M} \frac{\widetilde{\chi}_m}{|E_m|} \int_{E_m} g \, ds, \quad L^2(\partial\Omega) \to L^2(\partial\Omega). \tag{2.3}$$

Let us point out the different behavior of the two operators. Each current pattern is produced by integration over the extended electrodes and projection onto the area of the electrodes E_m. This is in contrast with the measurement process, where the integration is over the area of each electrode and the result is projected onto the extended electrodes as illustrated in Figure 2. In fact, P is the adjoint of J in $L^2(\partial\Omega)$, which can be checked by straightforward calculations.

The measurement that we obtain is then modeled as

$$g = P\mathcal{R}^\Gamma_\sigma \varphi = P\mathcal{R}_\sigma J\varphi. \tag{2.4}$$

The above construction is related to the gap model for EIT; see for instance [39] for a discussion of the different measurement models. As discussed in §2.2, to reconstruct the conductivity with the D-bar algorithm, we also need the ND map $\mathcal{R}_1$ corresponding to the case with the homogeneous conductivity $\sigma \equiv 1$; this can be obtained either by measurement (if possible) or careful simulation (e.g., using finite element model).

2.2. **Reconstructing from partial boundary measurements.** The classical full boundary data D-bar method is formulated in terms of the Dirichlet-to-Neumann map (DN map). If one is given Neumann-to-Dirichlet data, one can simply perform inversion of the ND measurement matrix to form the DN matrix and apply a D-bar algorithm. However, this approach does not extend to the case of partial boundary data, since the graphs of the ND and DN maps represent different subsets of the Cauchy data, hence inversion is not possible. Furthermore, even if one can perform numerical inversion of the ND matrix, the resulting matrix is not assured to coincide with the DN matrix. Also, these inverted partial boundary ND matrices tend to have large condition numbers, which alone will result in instabilities in the reconstruction process.

Here we very briefly review the background for the D-bar method; the interested reader is directed to [41] for further details. We begin with a change of variables that transforms the conductivity equation given in (1.1) into the 2-D Schrödinger equation with potential $q = \Delta\sqrt{\sigma}/\sqrt{\sigma}$. This Schrödinger equation is smoothly extended to the entire plane under the assumption that $\sigma \equiv 1$ in a neighborhood of $\partial\Omega$. We associate $(x, y) \in \mathbb{R}^2$

with points $z = x + iy \in \mathbb{C}$, introduce a complex frequency parameter $k \in \mathbb{C}$, and seek solutions $\psi(z,k)$ to the Schrödinger equation satisfying the asymptotic property $e^{-ikz}\psi(z,k) - 1 \in W^{1,\tilde{p}}(\mathbb{R}^2), \tilde{p} > 2$. The functions $\mu(z,k) := \psi(z,k)e^{-ikz}$ can then be shown to have the property $\mu(z,0) = \sqrt{\sigma(z)}$. It can further be shown that $\mu(z,k)$ can be recovered by solving a special D-bar equation involving the scattering transform $\mathbf{t}(k)$. The scattering transform can be thought of as a nonlinear Fourier transform of the Schrödinger potential q. In classical D-bar methods $\mathbf{t}(k)$ is computed using a reformulation to a boundary integral equation involving the DN map.

Our restrictions in the partial boundary setting motivate the reformulation of the D-bar method for ND measurement data and the direct use of the ND map as described in [22]. The first step involves computation of an approximate scattering transform from the ND map for $k \in \mathbb{C}$ by

$$\mathbf{t}^{\mathrm{ND}}(k) = \int_{\partial\Omega} \left(\partial_\nu\, e^{i\bar{k}\bar{z}}\right) (\mathcal{R}_1 - \mathcal{R}_\sigma)\, \partial_\nu\, e^{ikz} ds(z). \tag{2.5}$$

For the chosen geometry, i.e. the unit disk $\Omega = \mathbb{D}$, this can be simply evaluated as

$$\begin{aligned}\mathbf{t}^{\mathrm{ND}}(k) &= \int_{\partial\Omega} i\bar{k}\bar{z}e^{i\bar{k}\bar{z}}(\mathcal{R}_1 - \mathcal{R}_\sigma)ikze^{ikz}ds(z)\\ &= |k|^2 \int_{\partial\Omega} \bar{z}e^{i\bar{k}\bar{z}}(\mathcal{R}_\sigma - \mathcal{R}_1)ze^{ikz}ds(z).\end{aligned}$$

In practice, noise in the measurement data leads to blowup (in magnitude) of the scattering data for large $|k|$ frequencies. Therefore we employ a low-pass filtering of the scattering data by only computing $\mathbf{t}^{\mathrm{ND}}$ via (2.5) on a disk of radius $R > 0$. In the case of full boundary data, low-pass filtering of the scattering data was proven in [35] to be a regularization strategy, where the radius of the truncation depends on the noise level of the measurement data. For the partial boundary data case, a non-uniform truncation in the form of a thresholding (through the parameter C_t) may be needed to control the blowup, leading to the following definition for the computation of the partial ND scattering data:

$$\mathbf{t}_R^{\mathrm{ND}}(k) = \begin{cases} \mathbf{t}^{\mathrm{ND}}(k) & \text{if } 0 < |k| \le R, \text{ and } \left|\Re\left(\mathbf{t}^{\mathrm{ND}}\right)\right|, \left|\Im\left(\mathbf{t}^{\mathrm{ND}}\right)\right| \le C_t \\ 0 & \text{else.}\end{cases} \tag{2.6}$$

The non-uniform truncation parameter C_t is largely influenced by the reduction to partial boundary ND data (see Figure 4 of [22]). In this work, the parameter C_t was set to the largest magnitude of the real or imaginary component of the blind scattering prior $\mathbf{t}^{\mathbf{PR}}$ described in Section 3 below.

The approximate scattering transform $\mathbf{t}_R^{\mathrm{ND}}$ is then used as a parameter in the D-bar equation

$$\overline{\partial}_k\, \mu_R(z,k) = \frac{1}{4\pi\bar{k}}\, \mathbf{t}_R^{\mathrm{ND}}(k) e_{-k}(z)\overline{\mu_R(z,k)}, \tag{2.7}$$

where $e_k(z) := e^{i(kz+\bar{k}\bar{z})}$. The D-bar equation (2.7) is solved independently for each $z \in \Omega$ via its equivalent integral formulation

$$\mu_R(z,k) = 1 + \frac{1}{(2\pi)^2} \int_{|k|\leq R} \frac{\mathbf{t}_R^{\mathrm{ND}}(k')}{\overline{k'}(k-k')}\, e_{-k'}(z)\overline{\mu_R(z,k')} dk_1' dk_2', \tag{2.8}$$

and the conductivity is then computed by simply evaluating

$$\sigma_R(z) = \mu_R(z,0)^2.$$

3. The a priori partial data method

In this section we outline the formulation of the new method, in which *a priori* information is embedded into the partial data D-bar algorithm, following the work in [1] which was developed for full-data reconstructions. This *a priori* data comes in the form of a conductivity distribution $\sigma^{\mathbf{PR}}$ that is approximated using previously known information. As discussed in §1, in many applications of EIT imaging, some prior information is known about the structure and electrical properties of the subject, and this information may be used to form $\sigma^{\mathbf{PR}}$, which is incorporated into the regularized D-bar method in two distinct ways. Throughout this section, some mathematical and computational details have been abbreviated; we refer the interested reader to [1] and to [41] for further details.

To begin, we form the Schrödinger potential

$$\mathrm{q}^{\mathbf{PR}}(z) = \frac{\Delta\sqrt{\sigma^{\mathbf{PR}}(z)}}{\sqrt{\sigma^{\mathbf{PR}}(z)}}. \tag{3.1}$$

In practice, we start with a piecewise-smooth *a priori* conductivity distribution $\sigma^{\mathbf{PR}}$, which is then mollified to be at least $\mathcal{C}^2$ smooth to compute (3.1). We define the function $\mu^{\mathbf{PR}}(z,k)$ to be the solution analogous to $\mu(z,k)$ that corresponds to $\sigma^{\mathbf{PR}}$. It is known from the theoretical work in [41] that for each fixed k, the function $\mu^{\mathbf{PR}}$ satisfies the Lippmann-Schwinger equation

$$\left[-\Delta - 4ik\,\overline{\partial}_z + \mathrm{q}^{\mathbf{PR}}(z)\right]\mu^{\mathbf{PR}}(z,k) = 0, \tag{3.2}$$

where $\mu^{\mathbf{PR}}(\cdot,k) - 1 \in W^{1,\tilde{p}}(\mathbb{R}^2)$ for some $2 < \tilde{p} < \infty$. The function $\mu^{\mathbf{PR}}$, obtained by solving (3.2), now encodes the *a priori* information.

The first way $\mu^{\mathbf{PR}}$ is incorporated into the method involves extending the radius of admissible scattering data from R to $R_2 \geq R$, by appending an annulus of stable prior scattering data outside the disk where $\mathbf{t}_R^{\mathrm{ND}}$ is supported. To this end, we compute the *a priori* scattering data $\mathbf{t}^{\mathbf{PR}}$ using the alternate formulation

$$\mathbf{t}^{\mathbf{PR}}(k) = \int_{\mathbb{R}^2} e_k(z)\,\mu^{\mathbf{PR}}(z,k)\,\mathrm{q}^{\mathbf{PR}}(z)\,dz, \tag{3.3}$$

which avoids computation of the ND map corresponding to $\sigma^{\mathbf{PR}}$. See [22] for a derivation of the ND form of the scattering transform as in (2.5) from

a definition analogous to (3.3). The extended scattering data is then formed as

$$\mathbf{t}_{R,\,R_2}(k) := \begin{cases} \mathbf{t}^{\mathrm{ND}}(k) & 0 < |k| \leq R \\ \mathbf{t}^{\mathbf{PR}}(k) & R < |k| \leq R_2 \\ 0 & \text{else.} \end{cases} \tag{3.4}$$

If an additional threshold parameter is used to truncate the measurement scattering data $\mathbf{t}^{\mathrm{ND}}$ as in the formulation (2.6), the above definition of $\mathbf{t}_{R,\,R_2}$ may be modified so that, for any k such that $0 < |k| \leq R$, but either $\left|\Re(\mathbf{t}^{\mathrm{ND}})(k)\right| > C_t$ or $\left|\Im(\mathbf{t}^{\mathrm{ND}})(k)\right| > C_t$, we assign $\mathbf{t}_{R,\,R_2}(k) := \mathbf{t}^{\mathbf{PR}}(k)$. Furthermore, in the definition of $\mathbf{t}_{R,\,R_2}$, the influence of the prior on the resulting reconstruction can be controlled by choosing R_2 smaller or larger as desired. In particular, it should be noted that if an additional thresholding is used, then selecting $R_2 = R$ will not eliminate the prior completely from the definition of $\mathbf{t}_{R,\,R_2}$, but will result in a weak expression of the *a priori* data in the resulting reconstruction.

We next replace the asymptotic approximation $\mu \sim 1$ used in (2.8) with an improved approximation

$$\mu^{\mathrm{int}}(z) := \frac{1}{\pi R_2^2} \int_{|k| \leq R_2} \mu^{\mathbf{PR}}(z,k)\, dk \tag{3.5}$$

that approaches the asymptotic condition of 1 as $R_2 \to \infty$. We then choose a weighting parameter $\alpha \in [0,1]$ and for each $z \in \Omega$, solve a modified version of (2.8), using the extended scattering data $\mathbf{t}_{R,\,R_2}$ and asymptotic replacement term μ^{int}:

$$\begin{aligned} \mu_{R_2,\,\alpha}(z,k) = \alpha + (1-\alpha)\,\mu^{\mathrm{int}}(z) \\ + \frac{1}{(2\pi)^2} \int\limits_{|k| \leq R_2} \frac{\mathbf{t}_{R,\,R_2}(k')}{\overline{k'}(k-k')}\, e_{-k'}(z) \overline{\mu_{R_2,\,\alpha}(z,k')} dk_1' dk_2'. \end{aligned} \tag{3.6}$$

This equation is then solved for $\mu_{R_2,\,\alpha}$. The influence of the prior in the construction of $\mu_{R_2,\,\alpha}$ can be controlled by modifying the parameter α, and in fact, choosing $\alpha = 1$ will result in $\alpha + (1-\alpha)\,\mu^{\mathrm{int}}(z) = 1$, so that the only influence of the prior will be from the scattering data $\mathbf{t}_{R,\,R_2}$. Hence $\alpha = 0$ corresponds to the heaviest weighting of the μ^{int} term. Once we have obtained $\mu_{R_2,\,\alpha}$, the updated conductivity is recovered as

$$\sigma_{R_2,\,\alpha}(z) = \left(\mu_{R_2,\,\alpha}(z,0)\right)^2. \tag{3.7}$$

The steps of the new method are outlined in Figure 3. Note that steps 1a and 1b can be computed independently allowing for the *a priori* data computation to take place ahead of time offline, if desired. Furthermore, steps 1a and 1b are each parallelizable in k and step 2 is parallelizable in the spatial variable z, allowing for fast reconstructions.

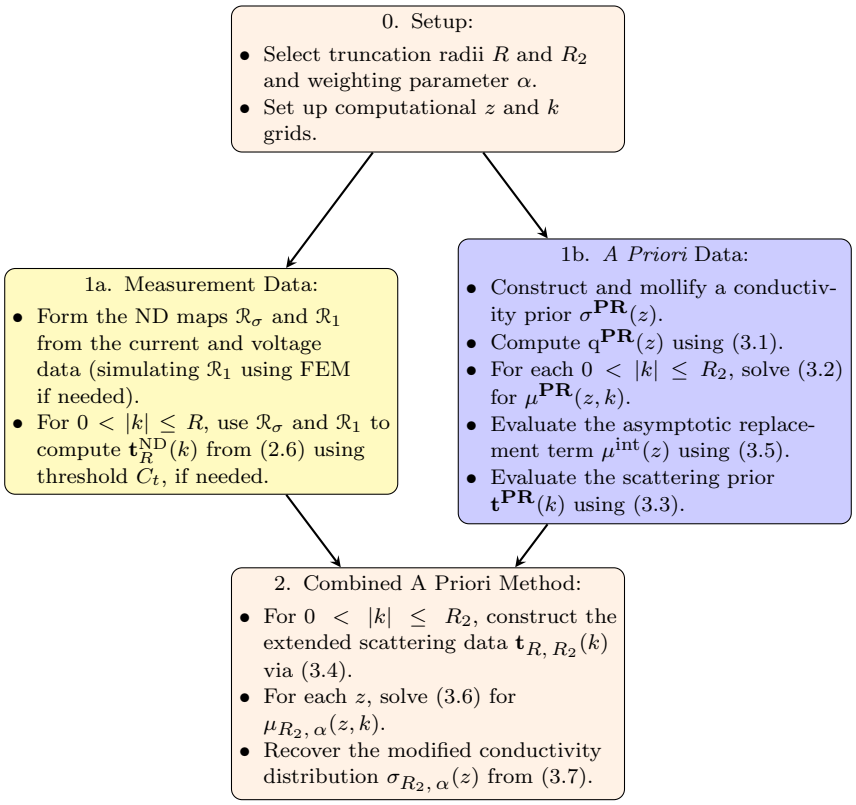

FIGURE 3. The *A Priori* D-bar Method with Partial Data

4. Computational results

We now demonstrate the effectiveness of the proposed method on simulated (noisy) EIT measurement data. We include two examples relevant to medical imaging (a simulated pneumothorax and a simulated pleural effusion) as well as an example of defect detection in a material, possibly relevant to an industrial setting. Figure 4 presents the phantoms used in the experiments, as well as the boundaries of their corresponding priors (represented by the white dots). Tables 1 and 2 give the conductivity values in each region of the phantoms and assigned priors. Note that a single prior is used for both thoracic examples, as it corresponds to a healthy patient with no pathology. Only information known with high confidence is included: e.g., approximate locations of heart, lungs, aorta, spine, major inclusions, etc. To better visualize the nuances of the results and compare across examples, all conductivity reconstructions are displayed on a color scale maxed out at $\sigma = 2$, unless otherwise stated. The true maximum of each colormap is given in each image caption. The reader is advised to view the reconstructions on a computer screen if possible, to avoid color distortions and to visualize nuances likely masked in a printed version.

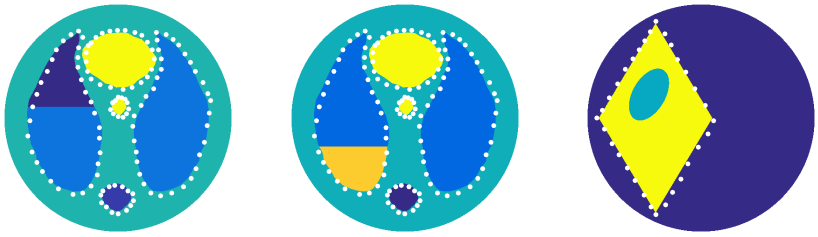

FIGURE 4. Phantoms used in numerical examples with the corresponding boundaries of the priors outlined by white dots. Note that for each example, the prior does not assume a pathology/defect. Left: A simulated pneumothorax occurring near the heart in the left lung. Middle: A simulated pleural effusion occurring away from the heart in the left lung. Right: An enclosed diamond with an ovular defect.

TABLE 1. Conductivity values of thoracic phantoms and assigned blind prior in S/m.

	Heart	Lungs	Pathology	Aorta	Spine	Background
Pneumothorax	2.0	0.5	0.15	2.0	0.25	1
Pleural Effusion	2.0	0.5	1.8	2.0	0.25	1
Prior	2.05	0.45	-	2.05	0.23	1

TABLE 2. Conductivity values of industrial phantom and assigned blind prior in S/m.

	Diamond	Inclusion	Background
Industrial	2.0	1.4	1
Prior	2.05	-	1

4.1. **Simulation of measurement data.** The construction for simulating the measurement data is described in §2.1. The ND map is represented using an orthonormal basis of $L^2(\partial\Omega)$, where $\Omega = \mathbb{D}$ is our chosen domain. The full boundary case assumes 32 equidistant electrodes around the boundary with a width of $|E_m| = \pi/32$ each. In the partial data case a certain number of electrodes are deactivated and not attached to the object. We explore three scenarios: 24, 20, and 16 active electrodes, corresponding to 75%, 62.5%, and 50% of the boundary accessible, respectively.

We simulate trigonometric current patterns for the basis functions $\varphi_n \in L^2(\partial\Omega)$ as

$$\varphi_n(\theta) = \frac{1}{\sqrt{\pi}} \begin{cases} \cos(n\theta) & \text{for } n > 0 \\ \sin((16-n)\theta) & \text{for } n > 16, \end{cases}$$

where $n \in \{1, \ldots, 31\}$. Note that for 32 electrodes, there are only 31 linearly independent basis functions [39]. Using the basis functions φ_n, the applied current values on the electrodes are produced by the nonorthogonal projection (2.2), as illustrated in Figure 2. The projected basis function is then used as a boundary condition for the conductivity equation (1.1). We solve the boundary value problem using a FEM solver for elliptic partial differential equations. The voltages on the electrodes are computed from the continuous solution $u|_{\partial\Omega}$ by applying the orthogonal projection (2.3) to the boundary trace, $g = Pu|_{\partial\Omega}$. Noisy measurement data was produced by adding 0.2% relative Gaussian zero-mean noise to the voltage data (independent for each current pattern and electrode). The measurement matrix $M \in \mathbb{R}^{31\times 31}$ was computed by evaluating the inner products for $n, m \in \{1, \ldots, 31\}$ as

$$M_{n,m} = (g_n, \varphi_m)_{L^2(\partial\Omega)} = (P\mathcal{R}_\sigma J\varphi_n, \varphi_m)_{L^2(\partial\Omega)}.$$

4.2. **Computation of the prior.** Figure 5(left) displays the piecewise-constant priors using the boundaries shown in Figure 4 and conductivity values in Tables 1 and 2. Note that the blind (healthy patient) thoracic prior is used for both the pneumothorax and pleural effusion examples, and neither prior (thoracic or industrial) assumes a pathology/defect. The conductivity priors were mollified (see Figure 5(right)) and the Schrödinger potential $\mathrm{q}^{\mathbf{PR}} = \frac{\Delta\sqrt{\sigma^{\mathbf{PR}}}}{\sqrt{\sigma^{\mathbf{PR}}}}$ computed. The Lippmann-Schwinger equation (3.2) was solved for each desired k and the associated scattering priors $\mathbf{t}^{\mathbf{PR}}$ and integral replacement terms μ^{int} formed via (3.3) and (3.5), respectively. Figure 6 shows the μ^{int} term for various extended radii R_2 for the blind thoracic prior.

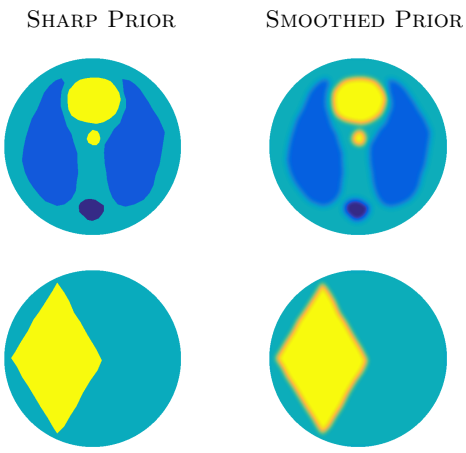

FIGURE 5. Blind priors used for the thoracic (top) and industrial (bottom) imaging examples. Take particular note that the priors do not assume any pathology/defect.

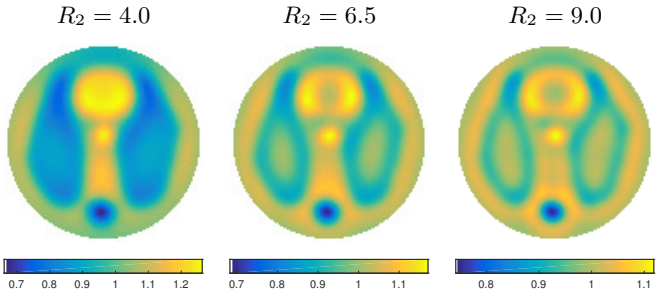

FIGURE 6. The real part of the μ^{int} data (shown in the z plane for $z \in \mathbb{D}$) corresponding to the blind *thoracic* prior given in Figure 5(top) computed from extended radii $R_2 = 4.0$, 6.5, and 9.0 in the k plane. Note that as the radius increases, the integral term approaches its asymptotic behavior of $\mu^{\text{int}} \sim 1$.

The combined scattering data $\mathbf{t}_{R,\,R_2}$ were then formed by combining $\mathbf{t}^{\text{ND}}$ (measurement data) with $\mathbf{t}^{\mathbf{PR}}$ (prior) as described in (3.4); see Figure 7 for an illustration.

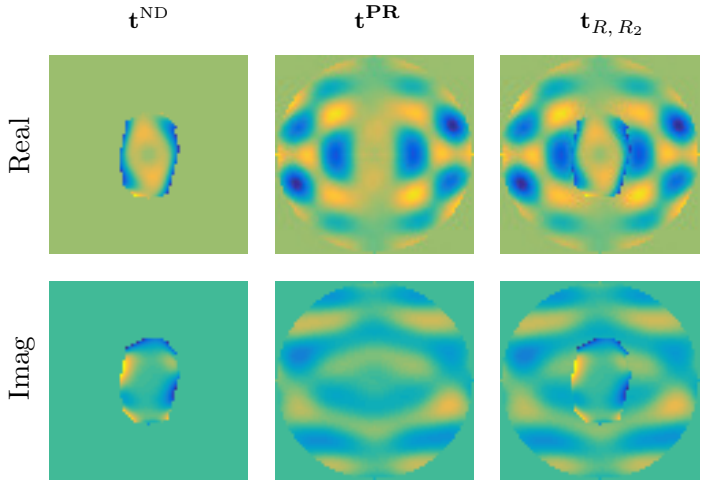

FIGURE 7. Scattering data corresponding to the pneumothorax example using the blind prior given in Figure 5(top). The original radius is $R = 4$ and extended radius $R_2 = 9$. All scattering data is plotted on the same scale (real and imaginary, respectively).

4.3. **Thoracic EIT imaging.** We explore two examples of interest in thoracic EIT imaging: a simulated pneumothorax and a simulated pleural effusion. In each case, we assume the same prior depicted in Figure 5(top).

Although our phantoms here are on circular domains, the purpose of this introductory work is to demonstrate the improvements the new method offers over the existing partial data results for direct D-bar methods in 2D [22, 20]. Our thoracic imaging examples that follow correspond to 75% and 62.5% access to the boundary of the patient, simulating ventral data for a patient lying on their back.

4.3.1. *Example 1: A Simulated Pneumothorax.* We begin with the simulated pneumothorax. Using only the partial data ND map, the conductivity σ^{ND} was recovered with a maximal radius of $R = 4$ and threshold of $C_t = 13.3528$, the maximum magnitude of the scattering prior (see Section 2.2). The reconstruction for 75% ventral access boundary data is shown at the top of Figure 8. The maximum value of the partial data reconstruction σ^{ND} is 1.4397 and the minimum is 0.2663.

While the partial data reconstruction σ^{ND} contains some quality information, the image exhibits fairly low spatial resolution. Using the prior depicted in Figure 5(top), which results in the corresponding extended scattering data (Figure 7) and asymptotic replacement term μ^{int} (Figure 6), the quality of the conductivity image improves greatly. Figure 8 shows the reconstructed conductivities $\sigma_{R_2,\,\alpha}$ using the new method, for varying extended radii $R_2 = 4.0, 6.5, 9.0$ and parameters $\alpha = 1, \frac{2}{3}, \frac{1}{3}, 0$. Recall that $\alpha = 1$ corresponds to the lowest weight of the μ^{int} term, while $\alpha = 0$ results in fullest expression of the prior. Notice that the reconstruction corresponding to $R_2 = 4.0$ and $\alpha = 1$ (the upper left corner of Figure 8), which represents $\mu^{\text{int}} = 1$ and merely augmenting the missing scattering data for $\mathbf{t}^{\text{ND}}$ to fill the k-disk of radius 4.0, already exhibits a significant improvement over the original partial data reconstruction σ^{ND}. As the value R_2 of the extended scattering radius increases, the pnuemothorax becomes more pronounced. Similarly, as the μ^{int} term is weighted more heavily, the organs separate nicely and again the pathology is striking. We remind the reader that no pathology has been included in the prior and hence the visible low conductive area in the upper left lung results purely from the measured data.

It is clear from the conductivity reconstructions in Figure 8 that there is a suspicious region in the upper left lung near the heart. This led us to update the spatial prior (in the spirit of [1]), as follows. We overlaid the organ boundaries of the blind thoracic prior on the $\sigma_{R_2,\,\alpha}$ reconstruction for $\alpha = 1$ and $R_2 = 9.0$ and employed a segmentation inside the left lung. The chosen values correspond to no weight given to the μ^{int} term. The segmentation was implemented, such that only the position of the suspected pathology (organ/region) and a division value are needed as inputs. Based on that information alone, the lung was segmented into two parts. The boundaries of the updated prior are displayed in Figure 9 using a division value of 0.25 S/m.

We then tested two new priors based on assigning the conductivity value of the suspicious region by using either the average value (0.2751 S/m) of the

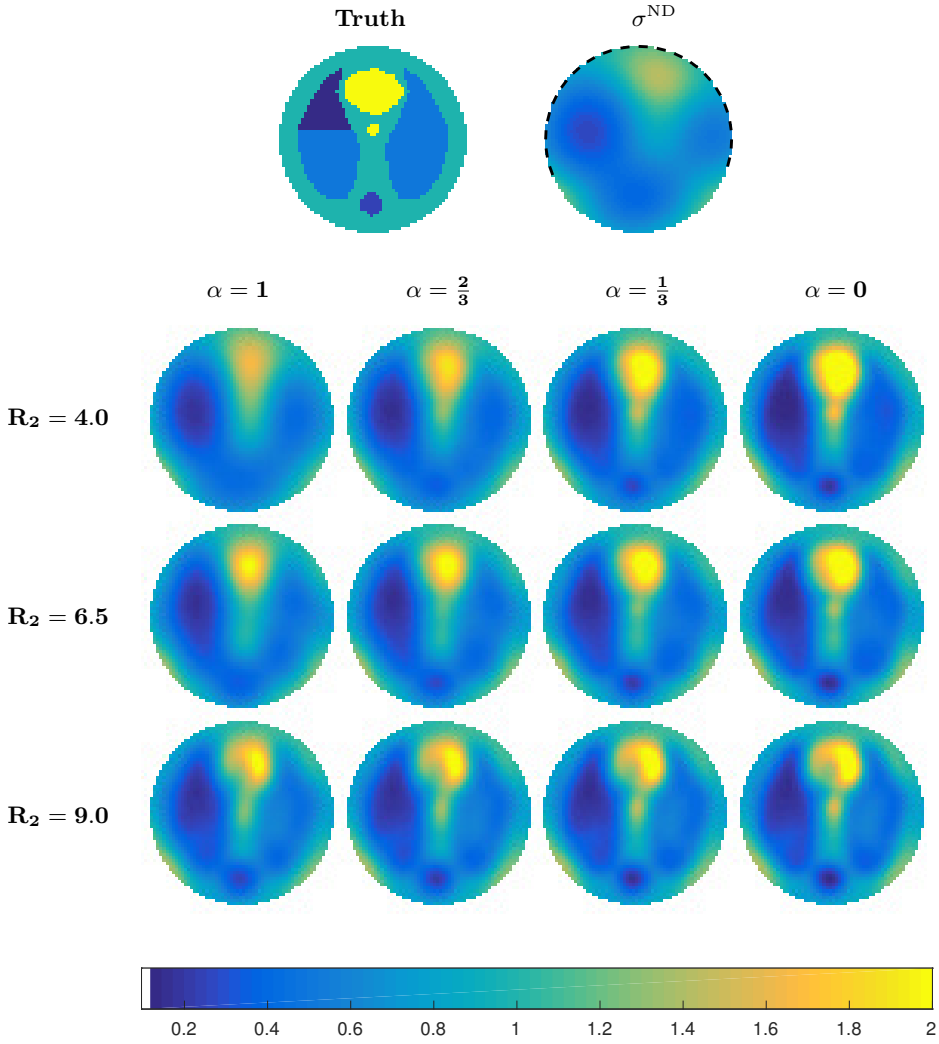

FIGURE 8. Pneumothorax example for 75% Ventral Data. TOP: The partial data ND D-bar reconstruction σ^{ND}. BOTTOM: The recovered conductivity $\sigma_{R_2,\alpha}$, shown for various regularization parameters R_2 and α using the blind thoracic prior. The maximum value is 2.49 and occurs for $R_2 = 4$ and $\alpha = 0$.

pixels in the region, or the minimum value (0.1754 S/m) of the pixels in the region since the value is clearly below the assigned value of 0.45, indicating an area of lower conductivity. In an effort to avoid bias, the average pixel value of the lower left lung (0.3894 S/m) was used in both new priors. The resulting conductivity reconstructions $\sigma_{R_2,\alpha}$ from the segmented priors are shown in Figure 10.

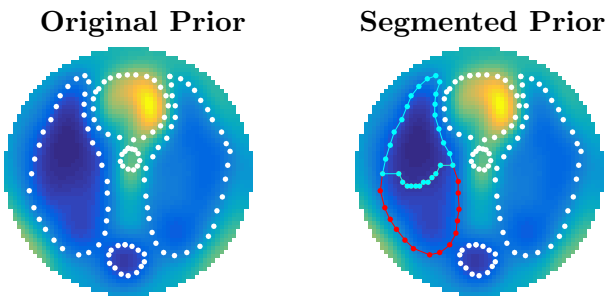

FIGURE 9. Left: Original prior. Right: Updated Pneumothorax prior. The left lung in the updated prior was segmented into two regions.

Figure 11 shows reconstructions using the blind thoracic prior with 62.5% ventral data, which corresponds to 20 active electrodes. The maximum value of the partial data reconstruction σ^{ND} is 1.4407 and the minimum is 0.2728. Figure 12 compares reconstructions from partial boundary data to full boundary data. The segmented priors for the full data case were extracted from $\sigma_{R_2,\alpha}$ using $R_2 = 9$ and $\alpha = 1$, with the average value (0.2657 S/m) or minimum value (0.1563 S/m) for the top region and the average value (0.4480 S/m) in the bottom. For 62.5% ventral data, the segmented priors were formed from $\sigma_{R_2,\alpha}$ for $R_2 = 4.0$ and $\alpha = 1$ with the extracted average value (0.3290 S/m) or minimum (0.2176 S/m) in the top region and the average pixel value (0.3724 S/m) in the lower lung region. Notice that the pneumothorax is clearly visible regardless of whether the average or minimum pixel value is used in the segmented prior. All of the reconstructions using the *a priori* method (original prior as well as from the segmented prior) are vast improvements over the partial data ND map D-bar image σ^{ND}, thus supporting the case for incorporating prior data directly into the method.

4.3.2. *Example 2: A Simulated Pleural Effusion.* Next we explore the thoracic example of a simulated pleural effusion in the lower region of the left lung. The recovered conductivity σ^{ND}, using only the 75% ventral data partial ND map, is shown in the top of Figure 13. The maximum value of the partial data reconstruction σ^{ND} is 1.5663 and the minimum is 0.3498. Notice that the fluid is visible as a region of higher conductivity, however the organs have little to no sharpness. Again, we employ the blind thoracic prior given in Figure 5(top) to produce the new conductivity reconstructions $\sigma_{R_2,\alpha}$ shown in Figure 13(bottom). As the blind prior is weighted more heavily, an artifact of higher conductivity between the lungs near the spine develops. This could be due to the prior trying to force the left lung to have a much lower conductivity in the lower region than it truly does. Nevertheless, we see that even the weakest expression of the prior ($R_2 = 4$

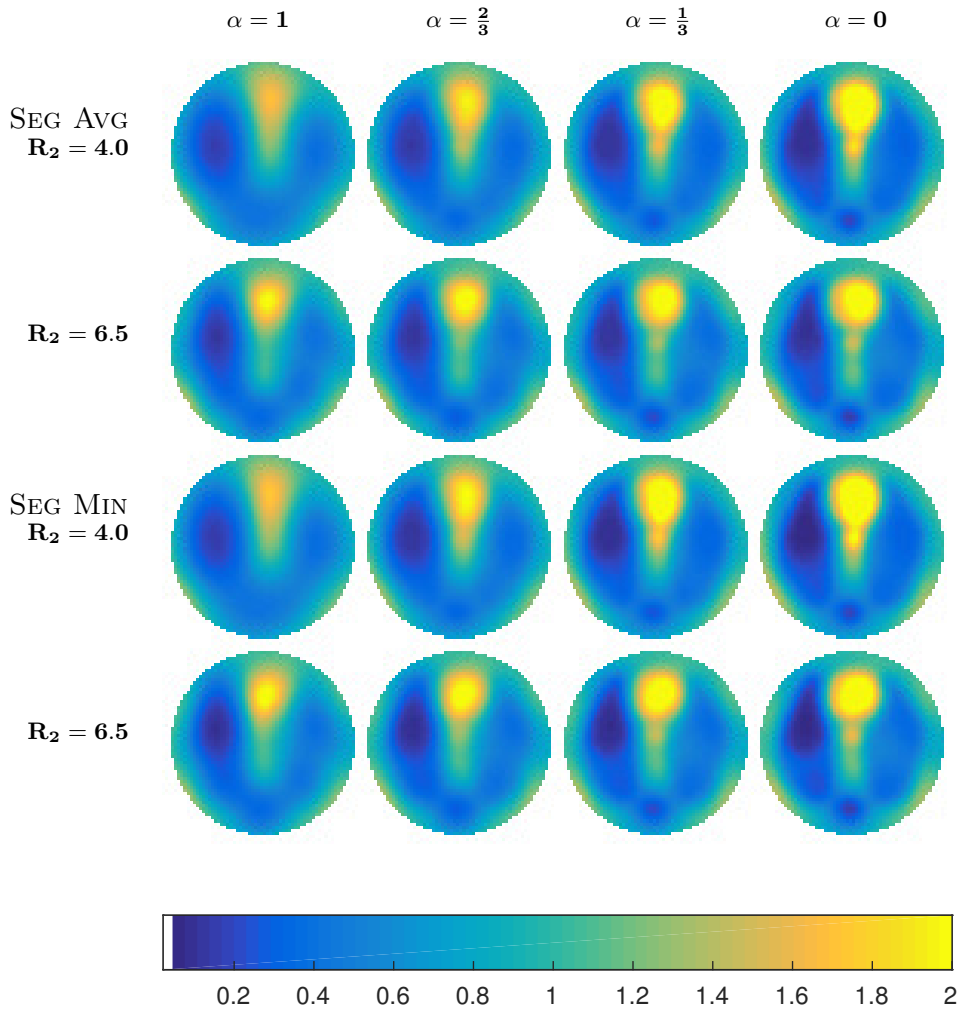

FIGURE 10. Pneumothorax example with 75% Ventral data and segmented prior. The corresponding partial data ND D-bar reconstruction σ^{ND} is shown in Figure 8. Here we display the recovered conductivity $\sigma_{R_2,\alpha}$ for $R_2 = 4, 6.5$ and various α using the SEG AVG or SEG MIN segmented thoracic priors. The maximum value is 2.70 and occurs in the $R_2 = 4$, $\alpha = 0$ recon using the SEG MIN prior.

and $\alpha = 1$) produces a conductivity image that is greatly improved over the partial data ND reconstruction σ^{ND}.

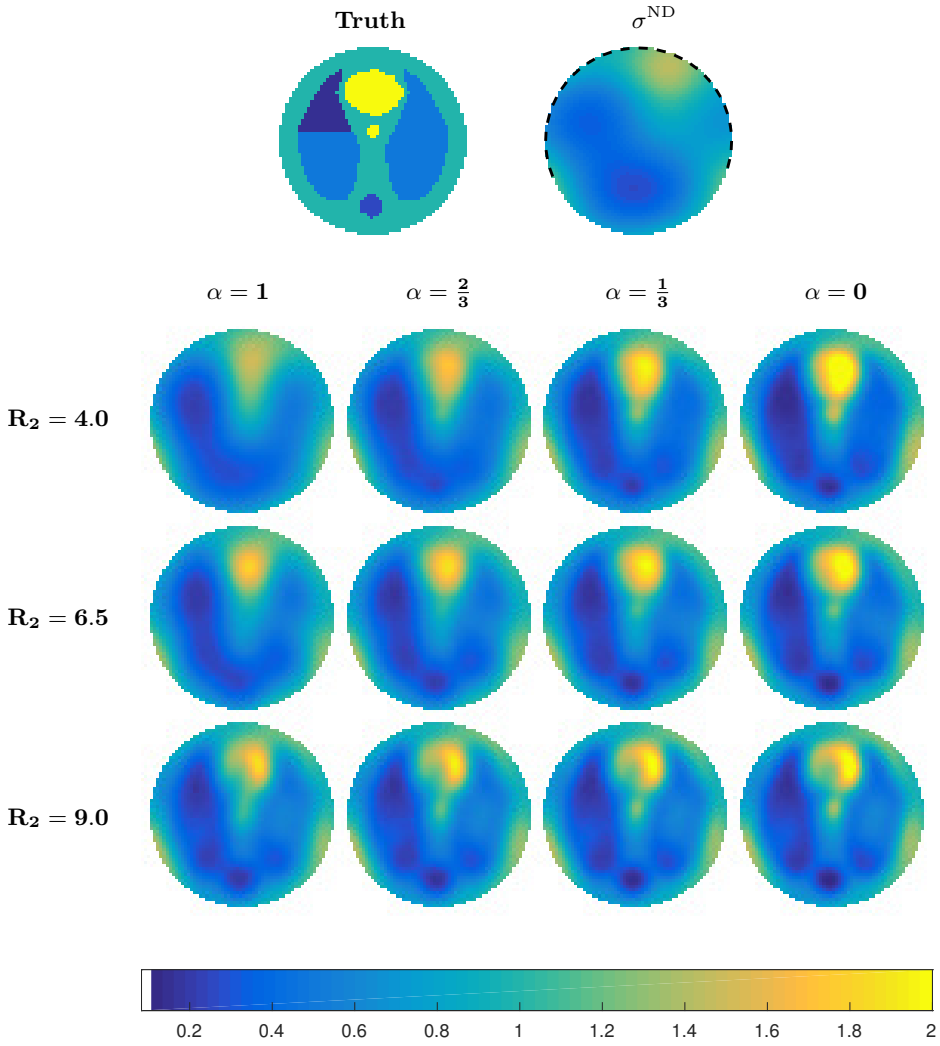

FIGURE 11. Pneumothorax example for 62.5% ventral data. TOP: The partial data ND D-bar reconstruction σ^{ND}. BOTTOM: The recovered conductivity $\sigma_{R_2,\alpha}$, using the blind thoracic prior. The maximum value is 2.25.

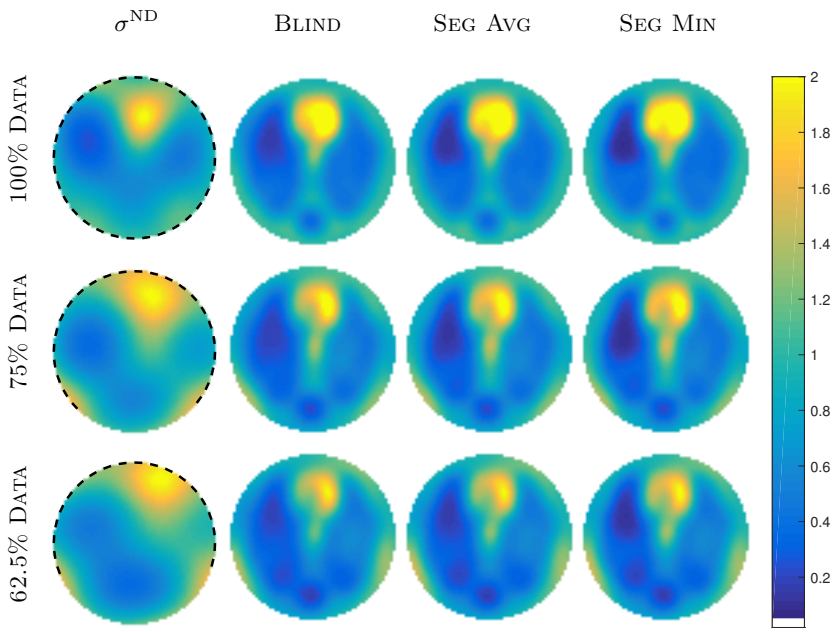

Figure 12. Pneumothorax Example. Results for $R_2 = 9.0$ and $\alpha = 0.67$. The maximum is 2.71 and occurs in the 100% boundary data, Blind prior reconstruction.

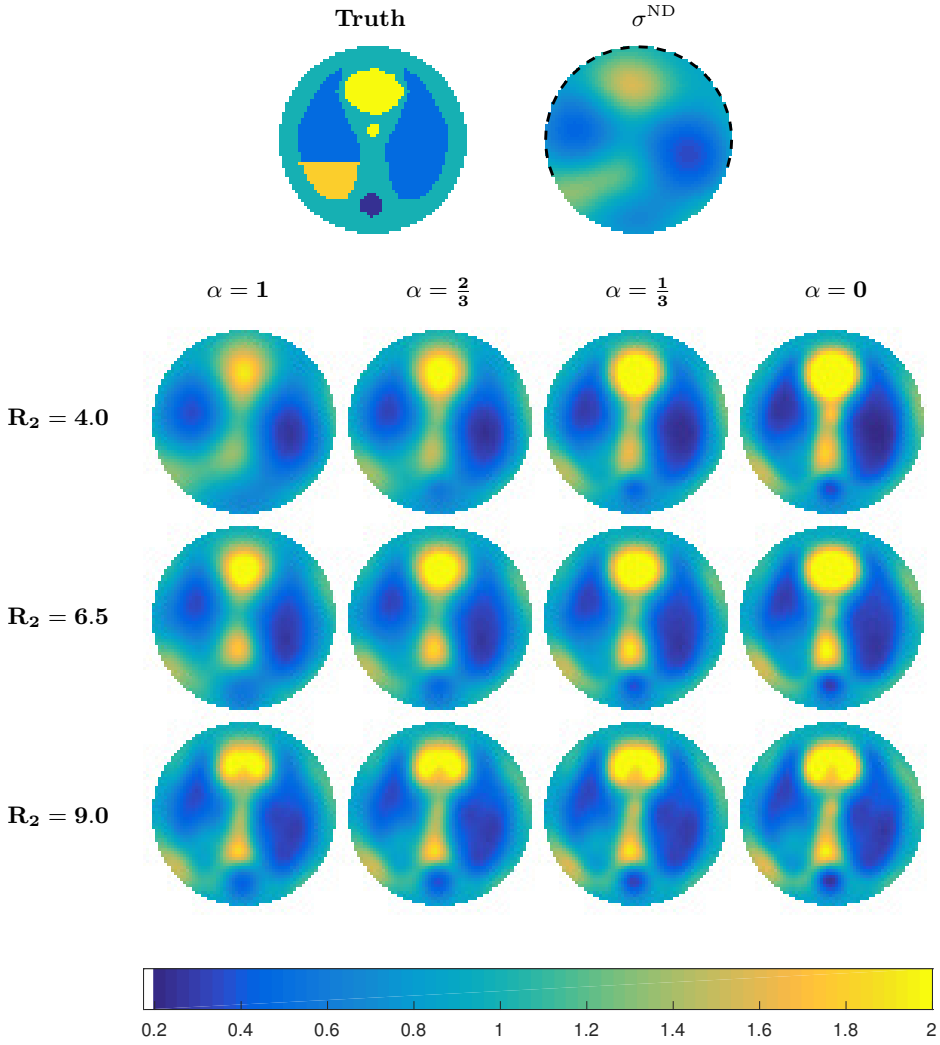

FIGURE 13. Pleural effusion example for 75% ventral data. TOP: The partial data ND D-bar reconstruction σ^{ND}. BOTTOM: The recovered conductivity $\sigma_{R_2,\alpha}$ using the blind thoracic prior. The maximum value is 2.90.

It is evident that there is a suspicious region in the left lung, indicating and update to the prior is needed (see [1] for a description of methods to update the prior). Using the $R_2 = 4$ and $\alpha = 1$ reconstruction, we overlaid the boundaries of the organs from the blind thoracic prior, and segmented the left lung (see Figure 14), as described in the pneumothorax example, using a division value of 0.9 S/m. New values for the bottom of the left lung were assigned from the average pixel value (1.1204 S/m) in the region, and the maximum pixel value (1.3444 S/m) in the region. The conductivity in the top of the left lung was set to the average pixel value in the region (0.6129 S/m) to avoid bias.

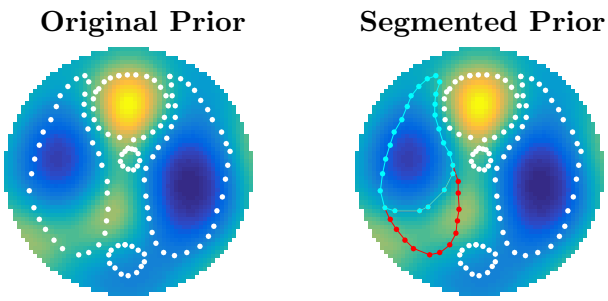

FIGURE 14. Left: Original prior. Right: Updated Pleural Effusion prior with the left lung segmented into two regions.

Following the last example, the extended scattering data was formed from the updated priors and the new μ^{int} terms computed. The new conductivities $\sigma_{R_2,\,\alpha}$ using the updated priors are shown in Figure 15. The reconstructions clearly demonstrate that by using either the average pixel value or maximum pixel value in the updated prior immensely improves the conductivity reconstructions. The previous artifact seen in the conductivity reconstruction using the blind thoracic prior (Figure 13) is reduced, especially when using the SEG MAX prior. This could be due to the area of higher conductivity now being allowed to be absorbed into the lower lung region where it belongs.

Figure 16 presents reconstructions from 62.5% ventral data and the blind thoracic prior. The maximum and minimum of the partial data reconstruction σ^{ND} are 1.48 and 0.42, respectively. Figure 17 compares reconstructions from partial boundary data to full boundary data. The segmented priors for the full data case were extracted from $\sigma_{R_2,\,\alpha}$ using $R_2 = 9$ and $\alpha = 1$, with the average value (1.2389 S/m) or maximum value (1.4796 S/m) for the top region and the average value (0.6077 S/m) in the bottom. The new segmented priors for 62.5% boundary data were created using $\sigma_{R_2,\,\alpha}$ for $R_2 = 4.0$ and $\alpha = 1$ with the extracted average value (0.8234 S/m) or maximum (1.0462 S/m) in the bottom region and the average pixel value (0.6372 S/m) in the top region. Note that for all levels of data, if the blind prior is used, a conductive artifact (not present in the D-bar reconstructions σ^{ND}) appears in the lower left of the image, near the bottom of the left lung, yet when the lung is segmented the artifact is significantly reduced, supporting the case for updating the prior and demonstrating what an artifact may look like when the prior is a bad match.

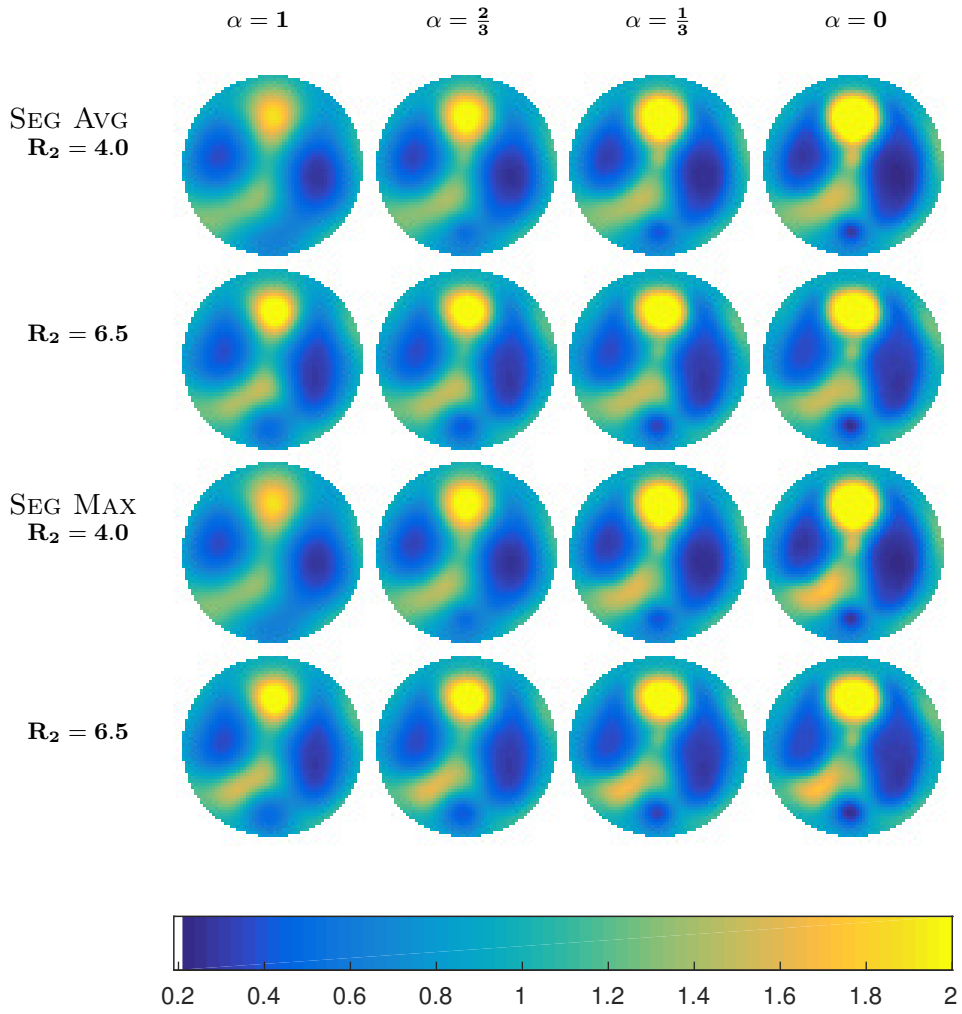

FIGURE 15. Pleural effusion example for 75% ventral data and segmented prior. The corresponding partial data ND D-bar reconstruction σ^{ND} is shown in Figure 13. Here we display the recovered conductivity $\sigma_{R_2,\alpha}$ for $R_2 = 4$, 6.5 and various α using the SEG AVG or SEG MAX segmented thoracic prior. The maximum value is 2.83 and occurs in the $R_2 = 4$, $\alpha = 0$ reconstruction using the SEG MAX prior.

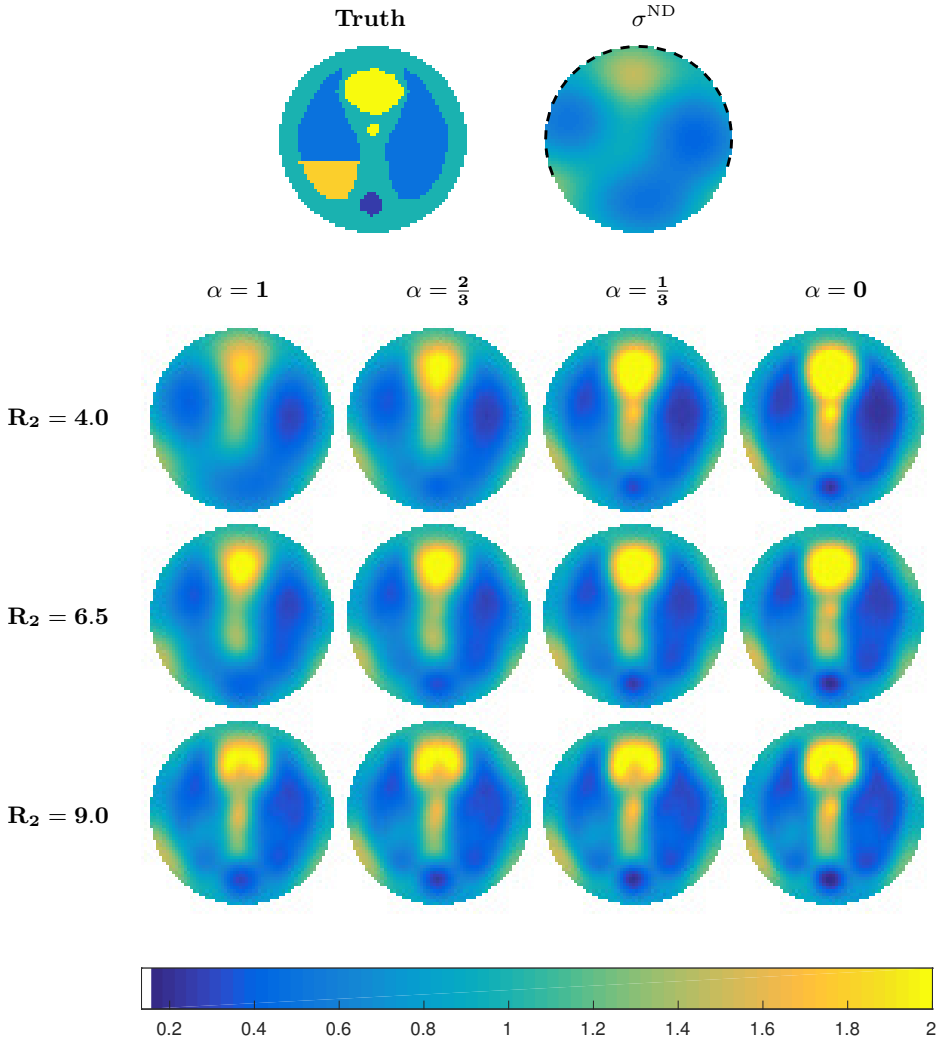

FIGURE 16. Pleural effusion example for 62.5% ventral data. The partial data ND D-bar reconstruction σ^{ND} is shown at the top. Below, the recovered conductivity $\sigma_{R_2,\alpha}$ is shown using the blind thoracic prior. The maximum value is 2.74.

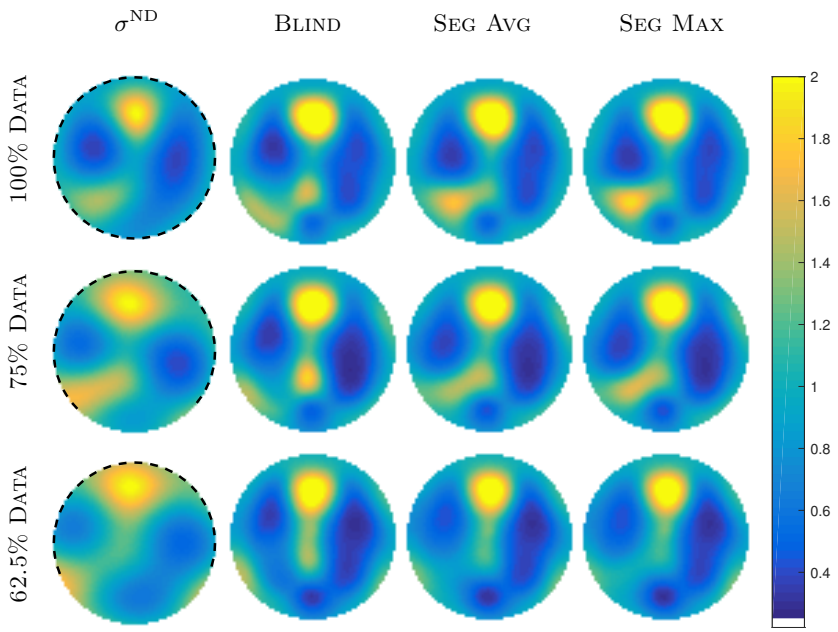

Figure 17. Pleural Effusion Example. Results for $R_2 = 6.5$ and $\alpha = 0.67$. The maximum is 2.65 and occurs in the 100% boundary data, Blind prior reconstruction.

4.4. **An industrial phantom with a defect.** Lastly we explore an example of potential interest to industry, a material with a defective region of lower conductivity. Here we compare D-bar ND reconstructions σ^{ND} from full, 75%, 62.5% and 50% boundary data (centered at $\pi/2$ degrees), to those including *a priori* data. The prior used here is shown in Figure 5(bottom) and assumes no defect. The D-bar reconstructions σ^{ND} were obtained as before using the (partial) ND map.

Figures 18 and 19 compare reconstructions for each level of boundary data with an extended scattering radius of $R_2 = 4$ and $R_2 = 6.5$, respectively. Observe that even with full boundary data the defect is not visible without the introduction of the prior (which, we remind the reader, does not assume any defect). As the prior is weighted more heavily, the diamond becomes better formed and the defect is clearly visible even in the first extension of the radius of the scattering data to $R_2 = 6.5$ (see Figure 19). For the partial data ND cases, we see that even the $R_2 = 4$ and $\alpha = 1$ conductivity $\sigma_{R_2,\alpha}$ reconstructions are significant improvements over the partial ND D-bar reconstructions σ^{ND}. For each level of boundary data, the defect becomes visible in the first increase of the radius of the scattering data. The μ^{int} correction term itself is not enough with only $R_2 = 4.0$ demonstrating the importance of both new pieces of information in the *a priori* method.

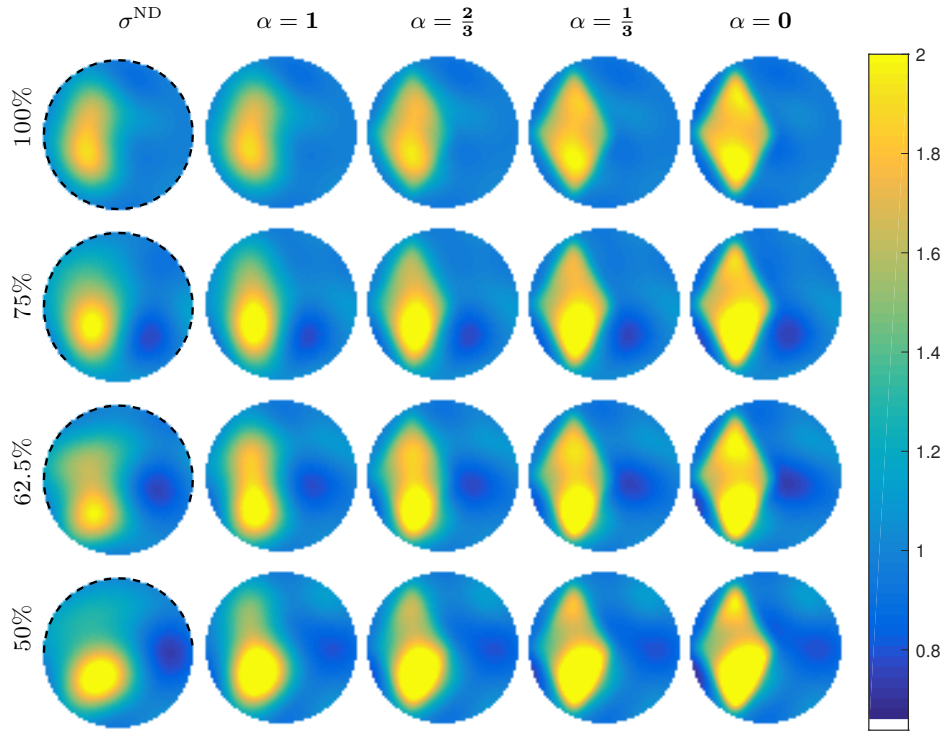

FIGURE 18. Industrial Example: From top to bottom, conductivity reconstructions $\sigma_{R_2,\alpha}$ for 100%, 75%, 62.5%, and 50% boundary data are presented with scattering radius $R_2 = 4$ and various weights α. The first column displays the σ^{ND} reconstructions that do not include any *a priori* information. The maximum value (3.12) occurs for the 50% data reconstruction with strongest weight $\alpha = 0$.

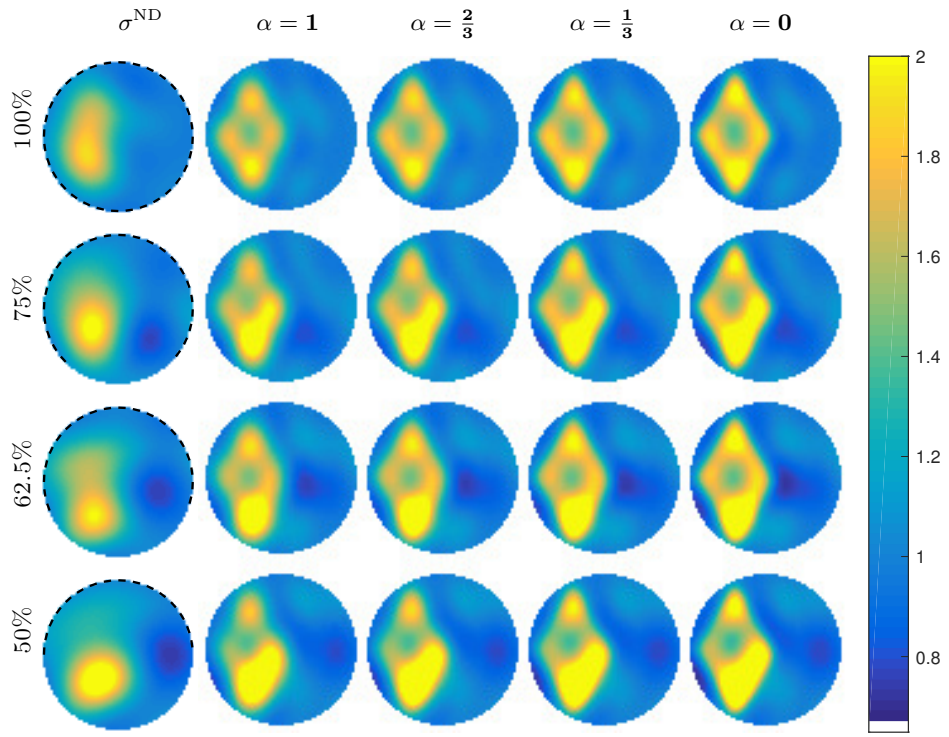

FIGURE 19. Industrial Example: From top to bottom, conductivity reconstructions $\sigma_{R_2,\alpha}$ for 100%, 75%, 62.5%, and 50% boundary data are presented with extended scattering radius $R_2 = 6.5$ and various weights α. The first column displays the σ^{ND} reconstructions that do not include any *a priori* information. The maximum value (3.13) occurs for the 50% data reconstruction with strongest weight $\alpha = 0$.

4.5. **Quantification of errors.** Our results demonstrate that conductivity reconstructions from partial boundary data using only $\mathbf{t}^{\mathrm{ND}}$ carry quality information, but suffer from a severe loss of spatial resolution. Incorporating *a priori* information in the reconstruction process can immensely enhance the visual impression of the image. The improvement is also clear from a decrease in the overall ℓ_2 relative errors (see Figure 20) and regional ℓ_2 relative errors (see Figure 21). In each plot, the error of the initial reconstruction σ^{ND} is displayed in the top left corner. Filling in the lost information in the scattering transform for the radius $R_2 = 4$ already increases accuracy (see $\alpha = 1$). In general, one can see that as the radius R_2 increases, or weighting of μ^{int} increases (i.e. α decreases from 1 to 0), the relative error in the overall reconstruction decreases. The extended radius $R_2 = 12$ is included here to demonstrate that only a slight improvement in the error may be expected for larger regularization radii. Reconstruction errors for all presented examples in §4 are displayed in Table 3.

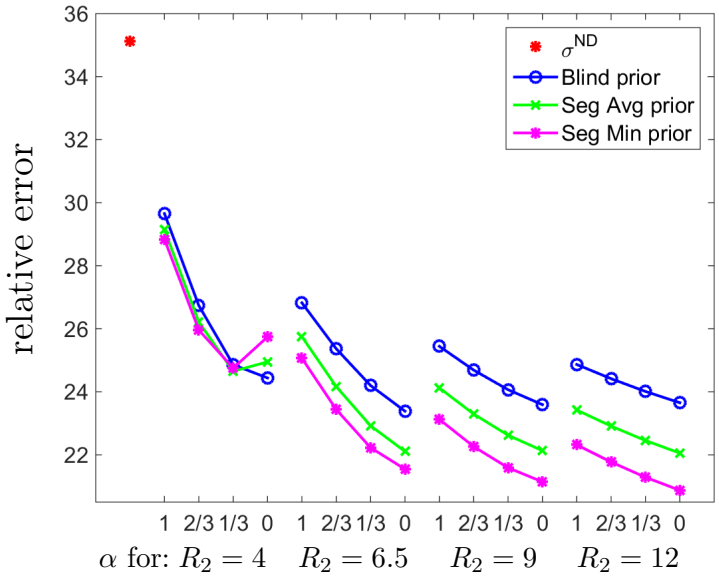

FIGURE 20. Relative ℓ_2-error of reconstructions from 75% ventral data of the pneumothorax example. The horizontal axis represents α-values for increasing regularization radii R_2. Recall that $\alpha = 0$ corresponds to the heaviest weighting of the μ^{int} term, while $\alpha = 1$ to the weakest expression of the prior. Errors from σ^{ND} are compared to the new reconstructions $\sigma_{R_2,\alpha}$ for the blind and segmented priors.

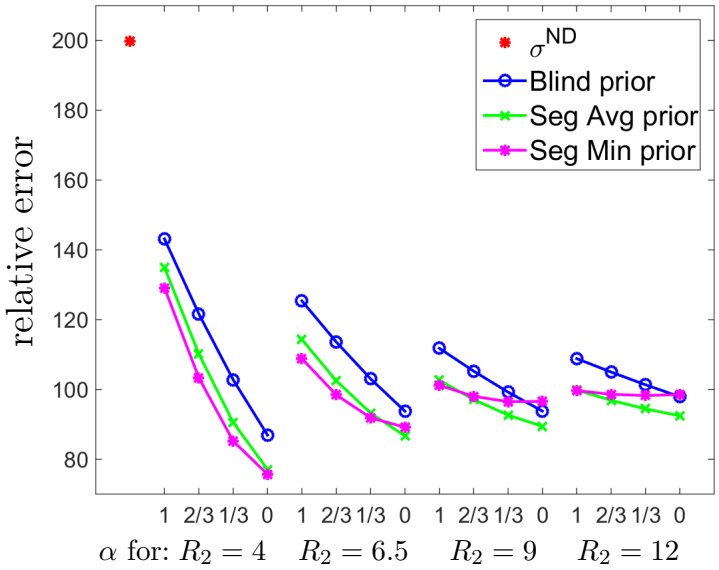

FIGURE 21. Relative ℓ_2-error in the lung region within the boundary of the pathology, for 75% ventral data for the pneumothorax example. The horizontal axis represents α-values for increasing regularization radii R_2.

5. Conclusions

We have presented a novel technique in which *a priori* information is embedded into an ND D-bar method for partial boundary EIT imaging of 2-D conductivities. The new method has great flexibility to be used with *a priori* information obtained in a variety of different ways, including previous CT or other scans, atlas matching (in the case of human imaging), or design schematics (in the case of industrial imaging), allowing for wide applicability.

To demonstrate the method's effectiveness in improving spatial resolution, we have presented the results of three test cases involving simulated partial boundary data with 0.2% relative added noise and varying percentages of available boundary data. The method was tested on both human thoracic phantoms with introduced pathologies, as well as an industrial phantom representing a nondestructive testing scenario. The success of the technique in these differing applications demonstrates the method's robustness and potential for adaptability to various real-world scenarios. In all cases presented, the new *a priori* method produced images exhibiting a significant increase in quality, specifically in sharpness of details and edges, over those from the partial data ND D-bar method. The blind priors only contain information that is likely to be known with high confidence based on a healthy or unblemished state. Nevertheless, changes to the subject that do no appear in the prior—such as the development of a pneumothorax or pleural

TABLE 3. Relative ℓ_2-errors (%) for the conductivity reconstructions from §4, for the extended regularization radii $R_2 = 4$ and 6.5.

	D-bar	$\mathbf{R_2 = 4}$				$\mathbf{R_2 = 6.5}$			
	Recon	$\alpha = 1$	$\alpha = \frac{2}{3}$	$\alpha = \frac{1}{3}$	$\alpha = 0$	$\alpha = 1$	$\alpha = \frac{2}{3}$	$\alpha = \frac{1}{3}$	$\alpha = 0$
Pneumothorax									
Blind Prior: 75%	35.13	29.65	26.74	24.86	24.44	26.82	25.36	24.20	23.39
Seg Avg Prior: 75%	35.13	29.14	26.22	24.65	24.95	25.75	24.16	22.92	22.11
Seg Min Prior: 75%	35.13	28.84	25.96	24.75	25.74	25.07	23.44	22.23	21.55
Blind Prior: 62.5%	38.95	32.71	30.02	28.06	27.12	30.12	28.74	27.56	26.63
Seg Avg Prior: 62.5%	38.95	32.33	29.62	27.83	27.30	29.43	27.99	26.78	25.84
Seg Min Prior: 62.5%	38.95	31.99	29.27	27.67	27.61	28.66	27.13	25.88	24.97
Pleural Effusion									
Blind Prior: 75%	27.40	24.82	24.43	25.94	29.23	25.44	25.54	26.13	27.20
Seg Avg Prior: 75%	27.40	24.24	22.27	21.88	23.33	22.40	21.47	20.96	20.90
Seg Max Prior: 75%	27.40	24.14	21.95	21.39	22.81	21.98	20.94	20.34	20.22
Blind Prior: 62.5%	32.56	29.80	29.22	30.00	32.21	29.34	29.10	29.20	29.67
Seg Avg Prior: 62.5%	32.56	29.18	27.66	27.22	28.08	27.53	26.80	26.35	26.21
Seg Max Prior: 62.5%	32.56	28.87	27.01	26.24	26.80	26.77	25.85	25.20	24.87
Industrial phantom									
Blind Prior: 100%	18.43	18.43	16.07	14.17	12.99	15.31	14.17	13.28	12.68
Blind Prior: 75%	18.46	17.91	16.10	14.99	14.80	15.23	14.42	13.93	13.80
Blind Prior: 62.5%	20.72	19.96	18.55	17.90	18.15	18.03	17.49	17.27	17.37
Blind Prior: 50%	22.14	21.24	20.25	20.04	20.70	19.68	19.34	19.31	19.60

effusion in human thoracic imaging, or the formation of a defect in industrial nondestructive evaluation—emerge with improved spatial resolution in the resulting reconstructions. This improvement was evident in all cases tested, even when available boundary data was decreased to 50% in the case of the industrial phantom. By updating the prior, based on information obtained from the EIT reconstructions, the conductivity reconstructions can be further improved. We have demonstrated how these updates may be accomplished using average regional conductivity values from the EIT reconstructions resulting in minimal introduced bias. In addition to conductivity reconstructions, we have provided relative ℓ_2 errors to help quantify the increase in spatial resolution resulting from the application of the method.

The ability to obtain high-quality EIT images in cases where only part of the boundary is accessible is important in a variety of applications. While an extensive study of how little partial data can be used to still produce informative images is outside the scope of this paper, we expect reasonable results near the area of data acquisition. Further study is also required to evaluate the method's clinical efficacy and industrial utility.

A thorough analysis of the computational expense associated with the method is also beyond the scope of this work, and the computations used in this paper were not optimized for speed. However, the method is parallelizable in either the k or z variable. Furthermore, computation of the

scattering prior $\mathbf{t}^{\mathbf{PR}}$ and the asymptotic replacement term μ^{int} may be performed in advance offline, and it may be possible to use the same prior (or a small set of similar priors) for all frames in a sequence of images. Thus, we expect that real-time imaging (as demonstrated in [13]) will be achievable with this method if a prior or priors are computed in advance.

References

[1] M. Alsaker and J. L. Mueller, *A D-bar algorithm with a priori information for 2-D Electrical Impedance Tomography*, SIAM J. on Imaging Sciences, 9 (2016), pp. 1619–1654.

[2] N. Avis and D. Barber, *Incorporating a priori information into the Sheffield filtered backprojection algorithm*, Physiological Measurement, 16 (1995), pp. A111–A122.

[3] U. Baysal and B. Eyüboglu, *Use of a priori information in estimating tissue resistivities - a simulation study*, Physics in Medicine and Biology, 43 (1998), pp. 3589–3606.

[4] D. Calvetti, P. J. Hadwin, J. M. Huttunen, D. Isaacson, J. P. Kaipio, D. McGivney, E. Somersalo, and J. Volzer, *Artificial boundary conditions and domain truncation in electrical impedance tomography. part i: Theory and preliminary results*, Inverse Problems & Imaging, 9 (2015), pp. 749–766.

[5] D. Calvetti, P. J. Hadwin, J. M. Huttunen, J. P. Kaipio, and E. Somersalo, *Artificial boundary conditions and domain truncation in electrical impedance tomography. part ii: Stochastic extension of the boundary map.*, Inverse Problems & Imaging, 9 (2015), pp. 767–789.

[6] E. Camargo, *Development of an absolute electrical impedance imaging algorithm for clinical use*, PhD thesis, University of São Paulo, 2013.

[7] F. J. Chung, *Partial data for the neumann-to-dirichlet map*, Journal of Fourier Analysis and Applications, 21 (2015), pp. 628–665.

[8] G. Cinnella, S. Grasso, P. Raimondo, D. D'Antini, L. Mirabella, M. Rauseo, and M. Dambrosio, *Physiological effects of the open lung approach in patients with early, mild, diffuse acute respiratory distress syndromean electrical impedance tomography study*, The Journal of the American Society of Anesthesiologists, 123 (2015), pp. 1113–1121.

[9] E. Costa, C. Chaves, S. Gomes, M. Beraldo, M. Volpe, M. Tucci, I. Schettino, S. Bohm, C. Carvalho, H. Tanaka, L. R.G., and M. Amato, *Real-time detection of pneumothorax using electrical impedance tomography*, Critical Care Medicine, 36 (2008), pp. 1230–1238.

[10] W. Daily and A. Ramirez, *Electrical imaging of engineered hydraulic barriers*, Geophysics, 65 (2000), p. 83.

[11] M. DeAngelo and J. L. Mueller, *2d D-bar reconstructions of human chest and tank data using an improved approximation to the scattering transform*, Physiological Measurement, 31 (2010), pp. 221–232.

[12] H. Dehghani, D. Barber, and I. Basarab-Horwath, *Incorporating a priori anatomical information into image reconstruction in electrical impedance tomography*, Physiological Measurement, 20 (1999), pp. 87–102.

[13] M. Dodd and J. L. Mueller, *A real-time D-bar algorithm for 2-D electrical impedance tomography data*, Inverse problems and imaging, 8 (2014), pp. 1013–1031.

[14] D. Ferrario, B. Grychtol, A. Adler, J. Sola, S. Bohm, and M. Bodenstein, *Toward morphological thoracic EIT: Major signal sources correspond to respective organ locations in CT*, Biomedical Engineering, IEEE Transactions on, 59 (2012), pp. 3000–3008.

[15] D. Flores-Tapia and S. Pistorius, *Electrical impedance tomography reconstruction using a monotonicity approach based on a priori knowledge*, in Engineering in Medicine and Biology Society (EMBC), 2010 Annual International Conference of the IEEE, Aug 2010, pp. 4996–4999.

[16] C. Grant, T. Pham, J. Hough, T. Riedel, C. Stocker, and A. Schibler, *Measurement of ventilation and cardiac related impedance changes with electrical impedance tomography*, Critical Care, 15 (2011), p. R37.

[17] G. Hahn, A. Just, T. Dudykevych, I. Frerichs, J. Hinz, M. Quintel, and G. Hellige, *Imaging pathologic pulmonary air and fluid accumulation by functional and absolute EIT*, Physiological measurement, 27 (2006), pp. S187–S198.

[18] M. Hallaji, A. Seppänen, and M. Pour-Ghaz, *Electrical impedance tomography-based sensing skin for quantitative imaging of damage in concrete*, Smart Materials and Structures, 23 (2014), p. 085001.

[19] S. J. Hamilton, J. L. Mueller, and M. Alsaker, *Incorporating a spatial prior into nonlinear d-bar EIT imaging for complex admittivities*, IEEE Trans. Med. Imaging (accepted), (2016).

[20] S. J. Hamilton and S. Siltanen, *Nonlinear inversion from partial data EIT: Computational experiments*, Contemporary Mathematics: Inverse Problems and Applications, (2014), pp. 105–129.

[21] B. Harrach and M. Ullrich, *Local uniqueness for an inverse boundary value problem with partial data*, in Proc. Amer. Math. Soc (accepted for publication), 2016.

[22] A. Hauptmann, M. Santacesaria, and S. Siltanen, *Direct inversion from partial-boundary data in electrical impedance tomography*, Inverse Problems (accepted), (2016).

[23] L. M. Heikkinen, M. Vauhkonen, T. Savolainen, K. Leinonen, and J. P. Kaipio, *Electrical process tomography with known internal structures and resistivities*, Inverse Probl. Eng., 9 (2001), pp. 431–454.

[24] T. Hermans, D. Caterina, R. Martin, A. Kemna, T. Robert, and F. Nguyen, *How to incorporate prior information in geophysical inverse problems-deterministic and geostatistical approaches*, in Near Surface 2011-17th EAGE European Meeting of Environmental and Engineering Geophysics, 2011.

[25] J. Hoła and K. Schabowicz, *State-of-the-art non-destructive methods for diagnostic testing of building structures – anticipated development trends*, Archives of Civil and Mechanical Engineering, 10 (2010), pp. 5–18.

[26] T. Hou and J. Lynch, *Electrical impedance tomographic methods for sensing strain fields and crack damage in cementitious structures*, Journal of Intelligent Material Systems and Structures, 20 (2009), pp. 1363–1379.

[27] N. Hyvönen, *Approximating idealized boundary data of electric impedance tomography by electrode measurements*, Mathematical Models and Methods in Applied Sciences, 19 (2009), pp. 1185–1202.

[28] N. Hyvönen, P. Piiroinen, and O. Seiskari, *Point measurements for a neumann-to-dirichlet map and the calderón problem in the plane*, SIAM Journal on Mathematical Analysis, 44 (2012), pp. 3526–3536.

[29] O. Imanuvilov, G. Uhlmann, and M. Yamamoto, *Inverse boundary value problem by partial data for the neumann-to-dirichlet-map in two dimensions*, arXiv preprint arXiv:1210.1255, (2012).

[30] D. Isaacson, J. L. Mueller, J. C. Newell, and S. Siltanen, *Reconstructions of chest phantoms by the D-bar method for electrical impedance tomography*, IEEE Transactions on Medical Imaging, 23 (2004), pp. 821–828.

[31] J. Kaipio, V. Kolehmainen, M. Vauhkonen, and E. Somersalo, *Inverse problems with structural prior information*, Inverse problems, 15 (1999), pp. 713–729.

[32] C. Karagiannidis, A. D. Waldmann, C. Ferrando Ortolá, M. Muñoz Martinez, A. Vidal, A. Santos, P. L. Róka, M. Perez Márquez, S. H. Bohm, and

F. Suarez-Spimann, *Position-dependent distribution of ventilation measured with electrical impedance tomography*, European Respiratory Journal, 46 (2015).

[33] K. Karhunen, A. Seppänen, A. Lehikoinen, P. J. M. Monteiro, and J. P. Kaipio, *Electrical resistance tomography imaging of concrete*, Cement and Concrete Research, 40 (2010), pp. 137–145.

[34] P. Kaup and F. Santosa, *Nondestructive evaluation of corrosion damage using electrostatic measurements*, Journal of Nondestructive Evaluation, 14 (1995), pp. 127–136.

[35] K. Knudsen, M. Lassas, J. Mueller, and S. Siltanen, *Regularized D-bar method for the inverse conductivity problem*, Inverse Problems and Imaging, 3 (2009), pp. 599–624.

[36] D. Liu, V. Kolehmainen, S. Siltanen, A.-m. Laukkanen, and A. Seppänen, *Estimation of conductivity changes in a region of interest with electrical impedance tomography*, Inverse Problems and Imaging, 9 (2015), pp. 211–229.

[37] D. Liu, V. Kolehmainen, S. Siltanen, and A. Seppänen, *A nonlinear approach to difference imaging in EIT; assessment of the robustness in the presence of modelling errors*, Inverse Problems, 31 (2015), p. 035012.

[38] J. Mueller and S. Siltanen, *Direct reconstructions of conductivities from boundary measurements*, SIAM Journal on Scientific Computing, 24 (2003), pp. 1232–1266.

[39] J. Mueller and S. Siltanen, *Linear and Nonlinear Inverse Problems with Practical Applications*, vol. 10 of Computational Science and Engineering, SIAM, 2012.

[40] E. K. Murphy and J. L. Mueller, *Effect of domain-shape modeling and measurement errors on the 2-d D-bar method for electrical impedance tomography*, IEEE Transactions on Medical Imaging, 28 (2009), pp. 1576–1584.

[41] A. I. Nachman, *Global uniqueness for a two-dimensional inverse boundary value problem*, Annals of Mathematics, 143 (1996), pp. 71–96.

[42] R. Novikov, *A multidimensional inverse spectral problem for the equation* $-\delta\psi + (v(x) - eu(x))\psi = 0$, Functional Analysis and Its Applications, 22 (1988), pp. 263–272.

[43] A. Pesenti, G. Musch, D. Lichtenstein, F. Mojoli, M. B. P. Amato, G. Cinnella, L. Gattinoni, and M. Quintel, *Imaging in acute respiratory distress syndrome*, Intensive Care Medicine, 42 (2016), pp. 686–698.

[44] H. Reinius, J. B. Borges, F. Fredén, L. Jideus, E. D. L. B. Camargo, M. B. P. Amato, G. Hedenstierna, L. A., and F. Lennmyr, *Real-time ventilation and perfusion distributions by electrical impedance tomography during one-lung ventilation with capnothorax*, Acta Anaesthesiologica Scandinavica, 59 (2015), pp. 354–368.

[45] A. Schlibler, T. Pham, A. Moray, and C. Stocker, *Ventilation and cardiac related impedance changes in children undergoing corrective open heart surgery*, Physiological Measurement, 34 (2013), pp. 1319–1327.

[46] A. Seppänen, K. Karhunen, A. Lehikoinen, J. Kaipio, and P. Monteiro, *Electrical resistance tomography imaging of concrete*, in Concrete Repair, Rehabilitation and Retrofitting II: 2nd International Conference on Concrete Repair, Rehabilitation and Retrofitting, 2009, pp. 571–577.

[47] S. Siltanen, J. Mueller, and D. Isaacson, *An implementation of the reconstruction algorithm of A. Nachman for the 2-D inverse conductivity problem*, Inverse Problems, 16 (2000), pp. 681–699.

[48] M. Soleimani, *Electrical impedance tomography imaging using a priori ultrasound data*, BioMedical Engineering OnLine, 5 (2006).

[49] M. Vauhkonen, D. Vadász, P. A. Karjalainen, E. Somersalo, and J. P. Kaipio, *Tikhonov regularization and prior information in electrical impedance tomography*, IEEE Transactions on Medical Imaging, 17 (1998), pp. 285–293.